

T -square resistivity without Umklapp scattering in dilute metallic $\text{Bi}_2\text{O}_2\text{Se}$

Jialu Wang^{1,2}, Jing Wu^{1,2}, Tao Wang^{1,2}, Zhuokai Xu^{1,2}, Jifeng Wu^{1,2}, Wanghua Hu^{1,2}, Zhi Ren^{1,2}, Shi Liu ^{1,2}, Kamran Behnia³ & Xiao Lin ^{1,2}✉

Fermi liquids (FLs) display a quadratic temperature (T) dependent resistivity. This can be caused by electron-electron (e-e) scattering in presence of inter-band or Umklapp scattering. However, dilute metallic SrTiO_3 was found to display T^2 resistivity in absence of either of the two mechanisms. The presence of soft phonons as possible scattering centers raised the suspicion that T^2 resistivity is not due to e-e scattering. Here, we present the case of $\text{Bi}_2\text{O}_2\text{Se}$, a layered semiconductor with hard phonons, which becomes a dilute metal with a small single-component Fermi surface upon doping. It displays T^2 resistivity well below the degeneracy temperature in absence of Umklapp and inter-band scattering. We observe a universal scaling between the T^2 resistivity prefactor (A) and the Fermi energy (E_F), an extension of the Kadowaki-Woods plot to dilute metals. Our results imply the absence of a satisfactory understanding of the ubiquity of e-e T^2 resistivity in FLs.

¹School of Science, Westlake University, 18 Shilongshan Road, 310024 Hangzhou, Zhejiang Province, China. ²Institute of Natural Sciences, Westlake Institute for Advanced Study, 18 Shilongshan Road, 310024 Hangzhou, Zhejiang Province, China. ³Laboratoire Physique et Etude de Matériaux (CNRS-Sorbonne Université-ESPCI Paris), PSL Research University, Paris 75005, France. ✉email: linxiao@westlake.edu.cn

Collision between electrons of a metal leads to a T -square resistivity. Postulated in 1930s by Landau and Pomeranchuk¹ and independently by Baber², this feature has been widely documented in elemental³ and strongly correlated⁴ metals. At sufficiently low temperature, their resistivity (ρ) follows this simple expression:

$$\rho = \rho_0 + AT^2 \quad (1)$$

The residual resistivity, ρ_0 , depends on defects but, A is an intrinsic property of the metal, found to scale with the electronic-specific heat^{3,4} in dense metals (i.e., those having roughly one carrier per formula unit). The quadratic temperature dependence of the phase space is a consequence of the fact that both participating electrons reside within a thermal window of the Fermi level.

In absence of a lattice, an electron–electron collision conserves momentum and cannot degrade the charge current. To generate finite resistivity, such collisions should transfer momentum to the lattice. There are two known mechanisms: either it is because there are multiple electron reservoirs unequally coupled to the lattice^{2,3}, or because the collision is an Umklapp event^{5,6}. In the first case, the two colliding electrons have distinct electron masses². Momentum transfer between these two distinct reservoirs sets the temperature dependence of resistivity, and the mass mismatch causes momentum leak to the lattice thermal bath. In the second case, one of the two colliding electrons is scattered to the second Brillouin zone and returns to the first one by transferring a unit vector of the reciprocal lattice (\mathbf{G}) of momentum to the lattice^{5,6}.

The observation of a T^2 resistivity in dilute metallic SrTiO₃ indicated, however, that our understanding of the microscopic foundations of this ubiquitous phenomenon is unsatisfactory⁷. SrTiO₃ is a cubic perovskite at room temperature. It is a quantum paraelectric and becomes a dilute metal upon introduction of a tiny concentration of mobile electrons⁸. Three concentric conducting bands centered at Γ point of the Brillouin zone are successively filled⁹. The quadratic temperature dependence of its electrical resistivity^{10,11} persists⁷ even when its Fermi surface shrinks to a single pocket¹² and none of the two mechanisms operate. However, it was more recently suggested that this enigmatic T -square resistivity may be caused by exotic mechanisms such as scattering by magnetic impurities¹³ or by two soft transverse optical phonons (See Supplementary Discussion)^{14,15}. Such soft phonons are known to play a decisive role in transport properties of the system, at least at high temperatures^{16–19}.

Here, we report on another dilute metal, doped Bi₂O₂Se. We show that it displays T^2 resistivity whilst the Hall carrier density (n) changes by two orders of magnitude and in absence of interband and Umklapp scattering. Moreover, there are no soft phonons and the T -square resistivity is restricted to temperatures well below the degeneracy temperature. The e–e origin of this T -square resistivity is unambiguous. Comparing the evolution of A with n and E_F in Bi₂O₂Se and SrTiO₃, we uncover a universal scaling between A and E_F in dense and dilute Fermi liquids. Our results imply that a proper microscopic theory of the link between electron–electron scattering and T -square resistivity is still missing.

Results

First-principle calculations of Bi₂O₂Se single crystal. Stoichiometric Bi₂O₂Se is a layered semiconductor with tetragonal crystal structure (anti-ThCr₂Si₂ phase) at room temperature²⁰, shown in Fig. 1a. Available Bi₂O₂Se single-crystals are metallic with extremely mobile carriers^{21–23}. The insulator is doped by unavoidable defects, such as Se or O vacancies and Se–Bi antisite defects^{24,25}.

According to density functional theory (DFT) calculations²⁴, the conduction band is centered at the Γ point of the Brillouin zone, following a parabolic dispersion (Fig. 1b and Supplementary Fig. 1). This has been revealed by angle-resolved photoemission spectroscopy (ARPES) measurements^{21,26}. The Fermi surface is an elongated ellipsoid (Fig. 1a) seen by quantum oscillations²⁶. The comparison of crystal and band structure between Bi₂O₂Se and SrTiO₃ is summarized in Supplementary Table 1.

Our DFT calculations of phonon spectrum for the tetragonal phase of Bi₂O₂Se are in agreement with what was reported previously^{27,28}. Figure 1c presents the phonon dispersion at ambient pressure. The absence of imaginary frequencies implies that the tetragonal phase is dynamically stable. Figure 1d–f shows the evolution of the calculated local potential and phonon frequencies with hydrostatic pressure. Clearly, the single-well local potential at ambient pressure is different from a quantum paraelectric, where the local potential is a shallow double-well and the ferroelectric phase is aborted due to quantum tunneling between two local minima of the well. In a quantum paraelectric, the soft mode is very sensitive to hydrostatic pressure. For example, in PbTe a well-known quantum paraelectric, the soft mode frequency almost triples by reducing the lattice constant (a) by 1%²⁹. In contrast, all three optical modes change moderately by reducing a , in Fig. 1f. The lowest mode (TO₁) hardens only by 20% by a similar reduction of a . We also note that a large negative pressure (≈ -5 GPa) is required to make the system ferroelectric. These observations rule out the proximity to a ferroelectric instability, excluding the presence of soft phonons.

Quadratic temperature dependence of resistivity. Figure 2a shows the temperature dependence of resistivity $\rho(T)$ in our Bi₂O₂Se samples with various n (See Supplementary Fig. 2, Supplementary Fig. 3 and Supplementary Table 2 for more information). We note that our data (obtained for $n < 1 \times 10^{19} \text{ cm}^{-3}$) smoothly joins what was recently reported for $n = 1.1 \times 10^{19} \text{ cm}^{-3}$ ³²². Upon cooling from room temperature to 1.8 K, resistivity decreases by two orders of magnitude, comparable to what is seen in doped quantum paraelectrics such as SrTiO₃, KTaO₃, and PbTe¹⁶.

Panels b–e of Fig. 2 document the low-temperature quadratic temperature dependence of resistivity. It persists down to the lowest temperatures in all the samples. Equation (1) holds below a characteristic temperature (dubbed T_{quad}). As seen in Fig. 2f, T_{quad} is an order of magnitude lower than T_F , the degeneracy temperature of the fermionic system (extracted from our study of quantum oscillations described below). The relevance of $T_{\text{quad}} \ll T_F$ inequality in Bi₂O₂Se contrasts with what was seen in SrTiO₃⁷. Only well below the degeneracy temperature, one expects the phase space of the fermion-fermion scattering to be quadratic temperature. Therefore, one reason to question the attribution of T -square resistivity to e–e scattering, which was raised in the case of SrTiO₃, is absent.

Figure 2g presents the evolution of the T^2 prefactor (A) with n for Bi₂O₂Se. For comparison, the relevant data for doped SrTiO₃ and KTaO₃ are also shown. In both cases, A decreases with increasing n . While $A(n)$ is more fluctuating in Bi₂O₂Se than in SrTiO₃, the two slopes ($\frac{n}{A} \frac{dA}{dn}$) are close to each other. At similar n , the magnitude of A differs by more than one order of magnitude lower. We will see below that this arises because of the difference in the magnitude of the effective electron mass, which sets the Fermi energy at a given carrier density.

Thus, Bi₂O₂Se is the second metallic system in which T -square resistivity is observed in presence of a single-component and small Fermi surface. The absence of multiple pockets leaves no place for interband scattering. The smallness of the Fermi surface excludes Umklapp events (See below for quantitative discussion).

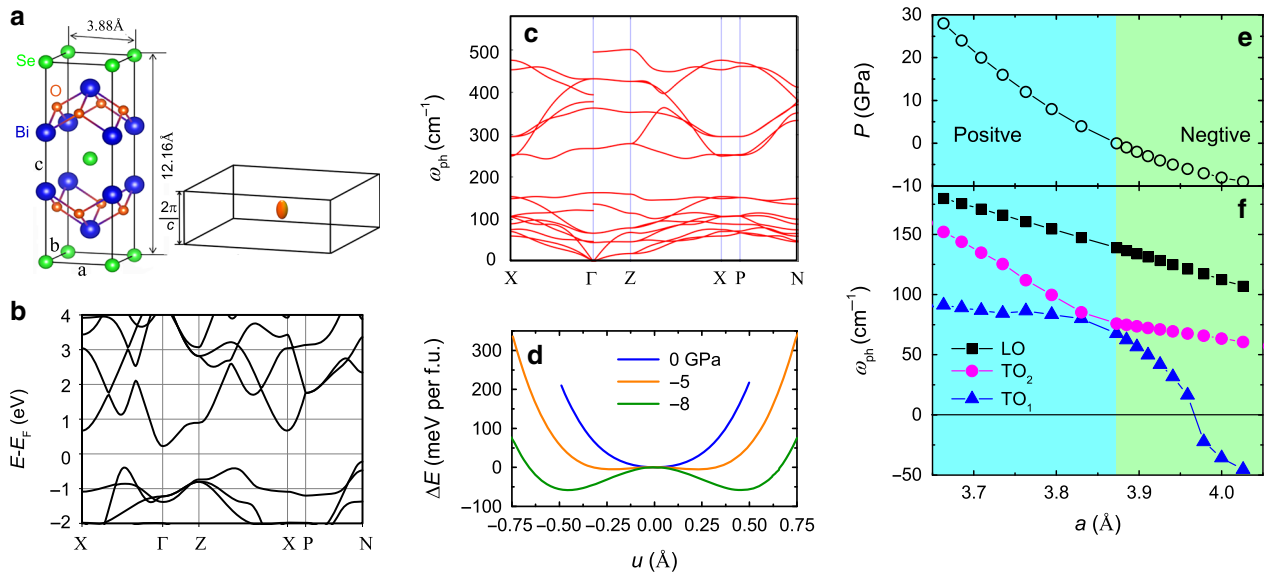


Fig. 1 Electronic and phonon properties of $\text{Bi}_2\text{O}_2\text{Se}$ from first-principle calculations. **a** Unit cell of the tetragonal phase and sketch of the ellipsoid Fermi surface at the Γ point of Brillouin zone. **b** Electronic band structures without spin-orbit coupling along high-symmetry lines of the Brillouin zone of the body-centered tetragonal unit cell. **c** Phonon dispersion at ambient pressure. **d** Local potential energy surface with respect to ion displacement along the lowest optical phonon mode, which changes from single-well to double-well by exerting large negative hydrostatic pressure. **e** One-to-one correspondence between the lattice parameter (a) and the hydrostatic pressure (P). **f** Frequency evolution of the three lowest optical modes with a , including two transverse modes: TO_1 (blue triangles) and TO_2 (magenta circles) and a longitudinal mode: LO (black squares). The lattice constant at ambient pressure (3.873 Å) is taken to be the optimized value from DFT calculations and the experimental lattice parameter is 3.88 Å.

Two features make the theoretical challenge thrown down by $\text{Bi}_2\text{O}_2\text{Se}$ more solid than the one presented by SrTiO_3 . First of all, since $T_{\text{quad}} \ll T_F$, one objection to associating T -square resistivity and e-e scattering vanishes. Moreover, the absence of any exotic soft phonons, rules out their possible role as scattering centers^{14,15}.

Having shown that T -square resistivity is present in $\text{Bi}_2\text{O}_2\text{Se}$ like in SrTiO_3 without objections ascribing it to e-e collisions, let us consider the relevance of the expression previously used⁷ for the T -square prefactor:

$$A = \frac{\hbar}{e^2} \left(\frac{k_B}{E_F} \right)^2 l_{\text{quad}} \quad (2)$$

Here, \hbar is Planck's constant divided by 2π , e is the electron charge, k_B is the Boltzmann constant and l_{quad} is a material-dependent characteristic length, which arises uniquely due to a dimensional analysis. Such an examination requires to know E_F at a given n . For this, we performed a detailed study of quantum oscillations.

Resistive quantum oscillations. Figure 3a, b shows that in presence of magnetic field, resistivity shows quantum oscillations with a single frequency for both in-plane and out-of-plane orientations of the magnetic field. When $n \approx 4.3 \times 10^{18} \text{ cm}^{-3}$, the oscillation frequency is $F_{\text{H}\parallel\text{c}} \approx 51 \text{ T}$ and $F_{\text{H}\parallel\text{ab}} \approx 93 \text{ T}$. This implies that the Fermi surface is an ellipsoid at the center of the Brillouin zone. The Fermi surface anisotropy $\alpha = \frac{F_{\text{H}\parallel\text{ab}}}{F_{\text{H}\parallel\text{c}}} = 1.8$. This is in excellent agreement with our theoretical calculations (Fig. 1b), which finds that the dispersion along Γ -X and Γ -Z with the value of anisotropy (α) differ by 1.75. Similar data for other samples are presented in the Supplementary Fig. 4 and summarized in Supplementary Table 3.

The volume of the ellipsoidal Fermi pocket implies a carrier concentration $n_{\text{sdH}} = 3.8 \times 10^{18} \text{ cm}^{-3}$, close to the Hall carrier

concentration. The numbers remain close to each other when $n > 10^{18} \text{ cm}^{-3}$ (see Supplementary Table 3). At very low densities, n_{sdH} starts to fall below n , which may indicate that the single Fermi sea begins to fall apart to isolated lakes due to insufficient homogeneity in doping.

The small size of the Fermi surface excludes the possible occurrence of Umklapp event, which requires a Fermi wave vector larger than one-fourth of the smallest reciprocal lattice vector, \mathbf{G} . For $\text{Bi}_2\text{O}_2\text{Se}$, the smallest \mathbf{G} is along c -axis, $\mathbf{G}_c = \frac{2\pi}{c} \approx 5.17 \text{ nm}^{-1}$, given the lattice constant $c = 12.16 \text{ Å}$ of the tetragonal unit cell. Then the threshold carrier density for Umklapp scattering (n_U) can be estimated to be $n_U = \frac{1}{3\pi^2} k_{\text{Fa}}^2 k_{\text{Fc}} = 3 \times 10^{19} \text{ cm}^{-3}$ with $k_{\text{Fc}} = \frac{\mathbf{G}_c}{4}$ and $\alpha = \frac{k_{\text{Fc}}}{k_{\text{Fa}}} \approx 1.8$ (k_{Fc} and k_{Fa} are Fermi wave vector along c -axis and a -axis). For $n < n_U$, no Umklapp scattering is expected, which includes our range of study and beyond.

Figure 3c shows how quantum oscillations are damped with increasing temperature. This allows us to extract the effective mass m^* using the Lifshitz-Kosevich (L-K) formula:

$$R_L = \frac{X}{\sinh(X)}, \quad X = \frac{\eta T m^*}{H} \quad (3)$$

where $\eta = \frac{2\pi^2 k_B}{eh}$. We find an in-plane effective electron mass $m_{\text{H}\parallel\text{c}}^* \approx 0.17 m_e$, in agreement with previous reports^{21,22,26}, and an out-of-plane mass $m_{\text{H}\parallel\text{ab}}^* \approx 0.25 m_e$ (m_e is the free electron mass). As expected, the ratio of these cyclotron masses is close to the ratio of the two ellipsoid axes.

Figure 3d shows $E_F = \frac{(\hbar k_{\text{Fab}})^2}{2m_{\text{H}\parallel\text{c}}^*}$ as a function of k_{Fab} (the in-plane wave vector). Each data point represents a different sample. As seen in Fig. 3e, the magnitude of the effective mass and Fermi surface anisotropy remain unchanged with doping. The data imply that the conducting band dispersion is parabolic. We also note that the effective mass resolved here ($m^* = 0.17 \pm 0.1 m_e$, see Table S1) is only 1.3 ± 0.1 larger than the DFT calculated bare

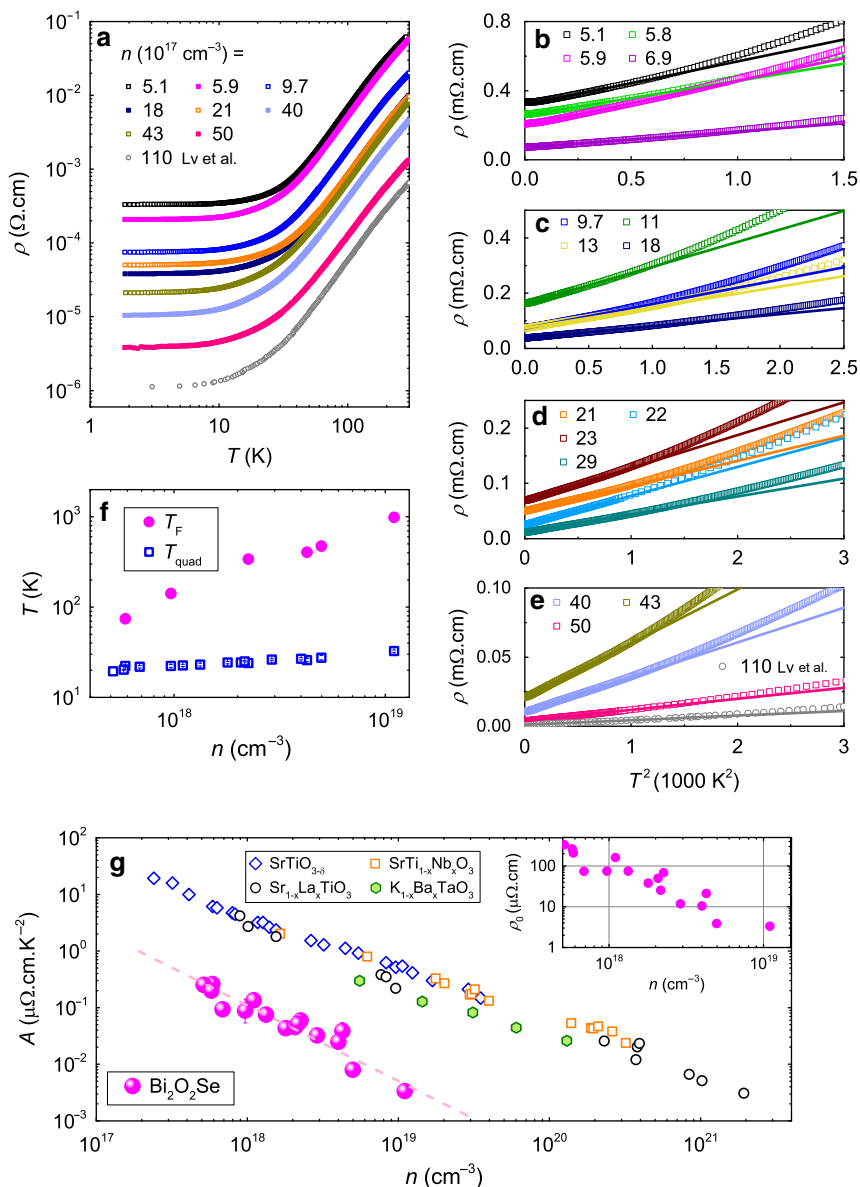


Fig. 2 Temperature-dependent resistivity of $\text{Bi}_2\text{O}_2\text{Se}$ at various Hall carrier concentrations (n). **a** Resistivity as a function of temperature from 1.8–300K on a Log-Log scale. The data at $n \approx 1.1 \times 10^{19} \text{ cm}^{-3}$ are from ref. ²². **b–e** The low- T resistivity as a function of quadratic temperature. The linear lines are fits by Eq. (1). **f** T_F and T_{quad} as a function of n . T_{quad} is a characteristic temperature above which the resistivity deviates from the T^2 behavior. T_F and T_{quad} are represented by solid magenta circles and open blue squares respectively. The error bars denote uncertainty in determining T_{quad} from **b–e**. **g** The slope of T^2 resistivity (A) as a function of n for $\text{Bi}_2\text{O}_2\text{Se}$: solid magenta circles, compared with doped SrTiO_3 ($\text{SrTiO}_{3-\delta}$: open blue diamonds, $\text{SrTi}_{1-x}\text{Nb}_x\text{TiO}_3$ ^{7,11}: open orange squares, and $\text{Sr}_{1-x}\text{La}_x\text{TiO}_3$ ¹⁰: open black circles) and $\text{K}_{1-x}\text{Ba}_x\text{TaO}_x$ ⁴⁵: solid olive hexagons. The dashed line is a guide to eyes. The inset shows the variation of residual resistivity with increasing n for $\text{Bi}_2\text{O}_2\text{Se}$.

mass of $m_b = 0.125m_e$. In contrast, in SrTiO_3 , band dispersion of the lower band is nonparabolic and there is a significant mass enhancement due to coupling to phonons^{7,11}. This comparison highlights the simplicity of the case of $\text{Bi}_2\text{O}_2\text{Se}$ where any polaronic effect seems to be absent.

Scaling between A and E_F . With the help of Fig. 3d, we can map n to E_F and translate the data of Fig. 2g in a new figure (Fig. 4a), which compares the evolution of A with E_F in $\text{Bi}_2\text{O}_2\text{Se}$ and in $\text{SrTiO}_{3-\delta}$. Remarkably, the two sets of data join each other. Because of the lightness of its electrons, $\text{Bi}_2\text{O}_2\text{Se}$ has a Fermi energy ten times higher than $\text{SrTiO}_{3-\delta}$ at the same carrier density.

In Fig. 4b, we include the new $\text{Bi}_2\text{O}_2\text{Se}$ data in a universal plot of A v.s. E_F . The data for other materials are taken from references^{7,8,30} and are summarized in Supplementary Table 4–6. Note that for all anisotropic conductors including $\text{Bi}_2\text{O}_2\text{Se}$, the plot shows the prefactor in the plane with the higher conductivity.

This plot is an extension of the original Kadowaki–Woods plot⁴ to dilute Fermi liquids. In a dense metal, the electronic-specific heat (in molar units) is an accurate measure of the Fermi energy. In a dilute metal, on the other hand, the molar units for atoms and electrons differ by orders of magnitude and therefore, one cannot use the electronic-specific heat as a measure of the Fermi energy.

Kadowaki and Woods observed originally that correlation between A and γ^2 in heavy-electron metals, such $A/\gamma^2 \approx 10 \mu\Omega$.

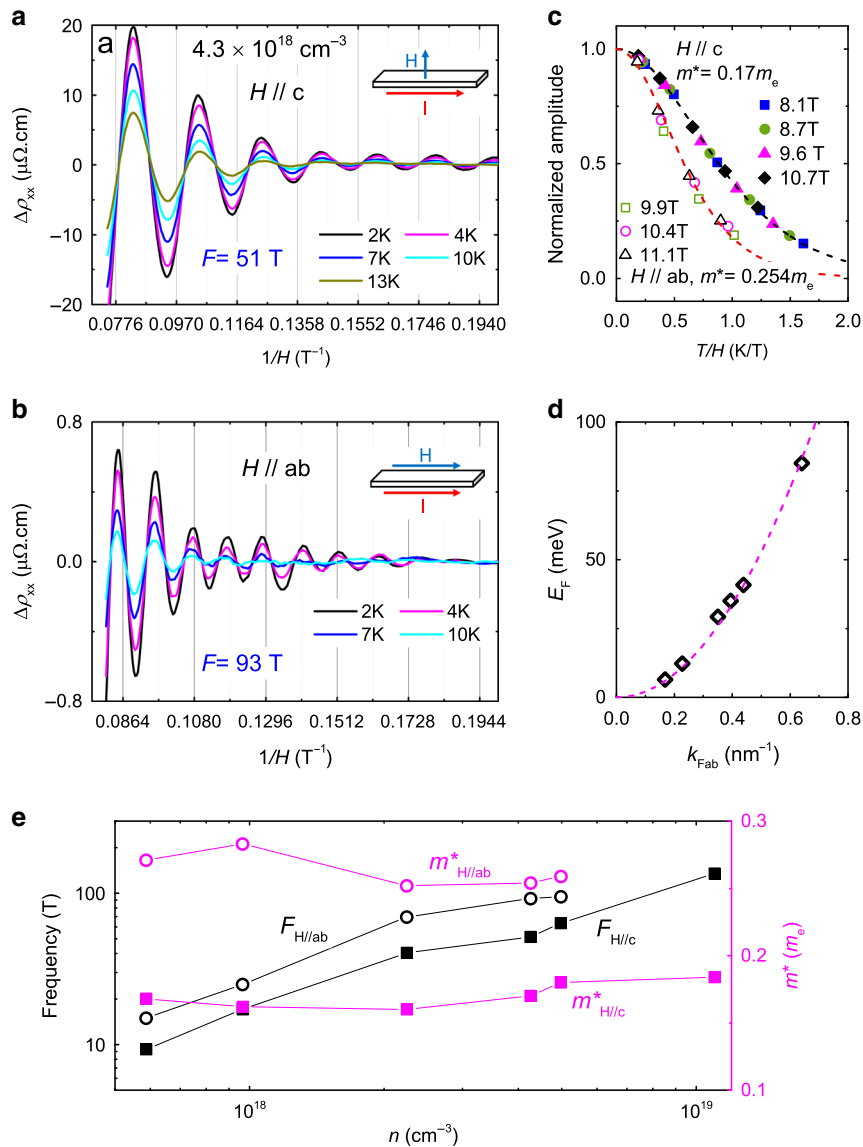


Fig. 3 Shubnikov-de Haas effect for $\text{Bi}_2\text{O}_2\text{Se}$ at $n \approx 4.3 \times 10^{18} \text{ cm}^{-3}$. **a, b** Resistive quantum oscillations as a function of inverse field ($1/H$) with $H \parallel c$ and $H \parallel ab$, respectively. $\Delta\rho = \rho - \rho_b$ where ρ_b is a fitted background of the magneto-resistance. **c** Normalized amplitude of oscillations as a function of T/H for two field directions. The dashed lines are the Lifshitz-Kosevich fits. **d** Fermi energy as a function of the in-plane Fermi wave vector for different samples, suggestive of a conducting band dispersion. The dashed line is a parabolic fit. **e** Evolution of the oscillation frequency (F) and the effective mass (m^*) with n in different samples for field along c -axis and ab -plane, respectively. $F_{H \parallel c}$ and $F_{H \parallel ab}$ are denoted by solid black squares and open black circles, respectively. $m_{H \parallel c}^*$ and $m_{H \parallel ab}^*$ are denoted by solid magenta squares and open magenta circles, respectively.

$\text{cm.K}^2.\text{mol}^2.\text{J}^{-24}$ and contrasted it with a similar ratio noticed by Rice in elemental metals ($A/\gamma^2 \approx 0.4 \mu\Omega.\text{cm.K}^2.\text{mol}^2.\text{J}^{-2}$)³, where γ is the electronic-specific heat coefficient. Subsequent studies³¹ brought new data indicating that these ratios define two rough and lower boundaries (and recently even ³He has been shown to be on the Kadowaki-Woods plot³²).

According to Fig. 4b, this 25-fold difference in the A/γ^2 magnitude is equivalent to a statement on the boundaries of l_{quad} , which lies between 1.6 and 40 nm across systems whose carrier concentration and Fermi energy differ by many orders of magnitude. This is in agreement with a recent observation by Kurita et al.³⁰. They put under scrutiny the correlation between A and the low-temperature slope of the Seebeck efficient (which remains a measure of the Fermi energy even in dilute systems³³) and found that in a variety of systems $l_{\text{quad}} \approx 4 \text{ nm}$ ³⁰.

l_{quad} is a phenomenological quantity coming out of dimensional analysis. Nevertheless, it is well-defined and equal to the product of the Fermi wave vector and the cross-section of electron-electron collision^{7,34}. This implies that its boundaries are meaningful and beg for an explanation.

Discussion

Most previous theoretical attempts focus on isolated cases and did not seek a global scenario. Let us consider briefly their relevance to our data. One scenario for T^2 resistivity, proposed decades ago, invokes inelastic electron-impurity scattering and its interplay with electron-phonon interaction³⁵⁻³⁷. Such an effect has been reported in several impure metals. It appears too weak to account for the T^2 term in $\text{Bi}_2\text{O}_2\text{Se}$ where $\frac{\Delta}{\rho_0} \sim 10^{-3} \text{ K}^{-2}$. Pal and co-authors proposed that non-Galilean invariant FLs can display T^2

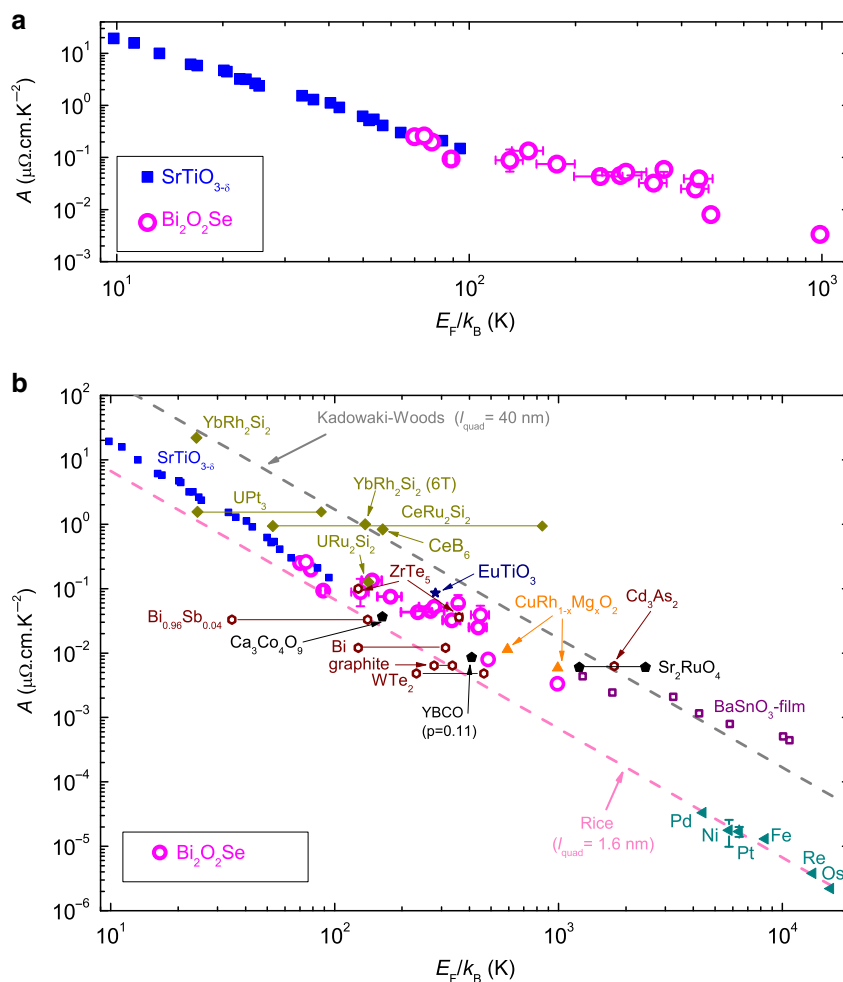


Fig. 4 Universal scaling between the slope of T^2 resistivity (A) and Fermi energy (E_F). **a** Variation of A with E_F on a Log–Log scale for $\text{Bi}_2\text{O}_2\text{Se}$: open magenta circles, compared to SrTiO_3 : solid blue squares⁷. **b** $A - E_F$ plot across various FLs, such as Metals: solid dark cyan triangles; strongly correlated metals including heavy Fermions: solid dark yellow diamonds and YBCO ($\text{YBa}_2\text{Cu}_3\text{O}_y$), Sr_2RuO_4 , $\text{Ca}_3\text{Co}_4\text{O}_9$: solid black pentagons; semimetals including Bi, $\text{Bi}_{0.96}\text{Sb}_{0.04}$, graphite, WTe_2 , Cd_3As_2 , and ZrTe_5 : open wine hexagons; doped semiconductors including $\text{Bi}_2\text{O}_2\text{Se}$, SrTiO_3 , BaSnO_3 : open purple squares, CuRhO_2 : solid orange triangles, EuTiO_3 : solid navy star^{7,8,30,46,47}. Most of the data are bounded by the two dashed lines set by Kadowaki–Woods and Rice, corresponding to a material-dependent length scale $l_{\text{quad}} \approx 40$ and 1.6 nm, respectively. The error bars for the data of $\text{Bi}_2\text{O}_2\text{Se}$ denote the uncertainty in determining A and E_F in processing the data. In solids with multiple Fermi surfaces, a horizontal bar links two data points representing the extrema in E_F .

resistivity even in the absence of Umklapp events³⁸. However, this scenario for T^2 resistivity does not expect it in a systems with parabolic dispersion such as $\text{Bi}_2\text{O}_2\text{Se}$. Quantum interference near a ferromagnetic quantum critical point (QCP) can induce a resistivity proportional to $T^2 \ln T$ ³⁹. This is inapplicable to $\text{Bi}_2\text{O}_2\text{Se}$, which is not close to any QCP. Lucas pointed to hydrodynamic flow of electrons in random magnetic fields as a possible source of T^2 resistivity¹³ in SrTiO_3 , speculating that oxygen vacancies can be magnetic there. Its relevance to a non-magnetic systems such as $\text{Bi}_2\text{O}_2\text{Se}$ is quite unlikely.

In summary, we find that the fermiology of dilute metallic $\text{Bi}_2\text{O}_2\text{Se}$ is such that interband or Umklapp scattering cannot happen. Nevertheless, there is a T^2 resistivity unambiguously caused by electron–electron scattering. We find a universal link between Fermi energy and the prefactor of T -square resistivity, which persists across various Fermi liquids. We conclude that a proper understanding of the microscopic origin of T -square resistivity in Fermi liquids is missing.

Methods

Sample growth. $\text{Bi}_2\text{O}_2\text{Se}$ poly-crystals were synthesized through solid state reaction with stoichiometric Bi (5N), Se (5N), and Bi_2O_3 (5N) powders of high purity.

The mixed materials are sealed in an evacuated quartz tube and heated in an oven at 823K for 24 h. The single-crystalline phase was obtained through the chemical vapor transport (CVT) method by using poly-crystals as precursors. The sealed quartz tubes were placed in a horizontal furnace at a temperature gradient from 1123 to 1023 K over one week. The resulting single-crystals are shiny and air-stable. Note that, we didn't use transport agents such as I_2 , in order to avoid unintentional doping. Samples with n below and above 10^{18} cm^{-3} are cleaved from two individual batches, respectively. Hence, we may expect a moderate inhomogeneous distribution of carrier concentrations in each sample.

Experiments. X-ray diffraction patterns were performed using a Bruker D8 Advanced X-ray diffractometer with $\text{Cu K}\alpha$ radiation at room temperature. The composition of samples was determined by an energy-dispersive X-ray (EDX) spectrometer affiliated to a Zeiss field emission scanning electron microscope (SEM). The transport measurements were done by a standard four-terminal method in Quantum Design PPMS-Dynacool equipped with 14T magnet. Ohmic contacts were obtained by evaporating gold pad to samples before attaching wires with silver paste.

DFT calculations. All first-principles calculations were carried out using density functional theory (DFT) as implemented in Quantum Espresso⁴⁰. The generalized gradient approximation (GGA) of Perdew–Burke–Ernzerhof revised for solids (PBEsol) type⁴¹ was used to describe the exchange–correlation energy. We used ultrasoft pseudopotentials from the Garrity, Bennett, Rabe, Vanderbilt (GBRV) high-throughput pseudopotential set⁴² and a plane-wave energy cutoff of 50 Ry and charge density cutoff of 250 Ry. The full phonon spectrum was calculated

using the supercell approach as implemented in phonopy⁴³ with the nonanalytical term correction at the Γ point included. As Bi is known for its strong spin-orbit coupling (SOC), the electronic band structure with SOC was calculated using the fully relativistic pseudopotentials taken from pslibrary (version 1.0.0)⁴⁴. Both electronic band structure and phonon spectrum were calculated along the high-symmetry lines of the Brillouin zone of a body-centered tetragonal unit cell.

Data availability

The data that support the findings of this study are included in this article and its supplementary information file and are available from the corresponding author upon reasonable request.

Received: 17 March 2020; Accepted: 14 July 2020;

Published online: 31 July 2020

References

- Landau, L. & Pomerantschuk, I. Über Eigenschaften der metalle bei sehr niedrigen Temperaturen. *Phys. Z. Sowjet* **10**, 649–653 (1936).
- Baber, W. G. The contribution to the electrical resistance of metals from collisions between electrons. *Proc. R. Soc. Lond. Ser. A* **158**, 383–396 (1937).
- Rice, M. J. Electron-electron scattering in transition metals. *Phys. Rev. Lett.* **20**, 1439–1441 (1968).
- Kadowaki, K. & Woods, S. B. Universal relationship of the resistivity and specific heat in heavy-Fermion compounds. *Solid State Commun.* **58**, 507–509 (1986).
- Yamada, K. & Yosida, K. Fermi liquid theory on the basis of the periodic Anderson Hamiltonian. *Prog. Theor. Phys.* **76**, 621–638 (1986).
- Maebashi, H. & Fukuyama, H. Electrical conductivity of interacting fermions. II Effects of normal scattering processes in the presence of Umklapp scattering processes. *J. Phys. Soc. Jpn.* **67**, 242–251 (1998).
- Lin, X., Fauqué, B. & Behnia, K. Scalable T^2 resistivity in a small single-component Fermi surface. *Science* **349**, 945 (2015).
- Collignon, C., Lin, X., Rischau, C. W., Fauqué, B. & Behnia, K. Metallicity and superconductivity in doped strontium titanate. *Ann. Rev. Cond. Mat. Phys.* **10**, 25–44 (2019).
- Lin, X. et al. Critical doping for the onset of a two-band superconducting ground state in $\text{SrTiO}_{3-\delta}$. *Phys. Rev. Lett.* **112**, 207002 (2014).
- Okuda, T., Nakanishi, K., Miyasaka, S. & Tokura, T. Large thermoelectric response of metallic perovskites: $\text{Sr}_{1-x}\text{La}_x\text{TiO}_3$ ($0 \leq x \leq 1$). *Phys. Rev. B* **63**, 113104 (2001).
- Van Der Marel, D., van Mechelen, J. L. M. & Mazin, I. I. Common Fermi-liquid origin of T^2 resistivity and superconductivity in n-type SrTiO_3 . *Phys. Rev. B* **84**, 205111 (2011).
- Lin, X., Zhu, Z., Fauqué, B. & Behnia, K. Fermi surface of the most dilute superconductor. *Phys. Rev. X* **3**, 021002 (2013).
- Lucas, A. Kinetic theory of electronic transport in random magnetic fields. *Phys. Rev. Lett.* **120**, 116603 (2018).
- Maslov, D. L. & Chubukov, A. V. Optical response of correlated electron systems. *Rep. Prog. Phys.* **80**, 026503 (2017).
- Epifanov, Y. N., Levanyuk, A. P. & Levanyuk, G. M. Interaction of carriers with TO-phonons and electrical conductivity of ferroelectrics. *Ferroelectrics* **35**, 199–202 (1981).
- Lin, X. et al. Metallicity without quasi-particles in room-temperature strontium titanate. *npj Quant. Mat.* **2**, 41 (2017).
- Zhou, J. J., Hellman, O. & Bernardi, M. Electron-phonon scattering in the presence of soft modes and electron mobility in SrTiO_3 perovskite from first principles. *Phys. Rev. Lett.* **121**, 226603 (2018).
- Zhou, J. J. & Bernardi, M. Predicting charge transport in the presence of polarons: the beyond-quasiparticle regime in SrTiO_3 . *Phys. Rev. Res.* **1**, 033138 (2019).
- Collignon, C., Bourges, P., Fauqué, B. & Behnia, K., Heavy non-degenerate electrons in doped strontium titanate. Preprint at <https://arxiv.org/abs/2001.04668> (2020).
- Boller, H. The crystal structure of $\text{Bi}_2\text{O}_2\text{Se}$. *Monatsh. Chem. Chem. Mon.* **104**, 916–919 (1973).
- Wu, J. X. et al. High electron mobility and quantum oscillations in non-encapsulated ultrathin semiconducting $\text{Bi}_2\text{O}_2\text{Se}$. *Nat. Nanotech.* **12**, 530–C534 (2017).
- Lv, Y. Y. et al. Electron-electron scattering dominated electrical and magnetotransport properties in the quasi-two-dimensional Fermi liquid single-crystal $\text{Bi}_2\text{O}_2\text{Se}$. *Phys. Rev. B* **99**, 195143 (2019).
- Wu, J. X. et al. Low residual carrier concentration and high mobility in 2D semiconducting $\text{Bi}_2\text{O}_2\text{Se}$. *Nano Lett.* **19**, 197–202 (2019).
- Fu, H. X., Wu, J. X., Peng, H. L. & Yan, B. H. Self-modulation doping effect in the high-mobility layered semiconductor $\text{Bi}_2\text{O}_2\text{Se}$. *Phys. Rev. B* **97**, 241203 (2018).
- Li, H. L. et al. Native point defects of semiconducting layered $\text{Bi}_2\text{O}_2\text{Se}$. *Sci. Rep.* **8**, 10920 (2018).
- Chen, C. et al. Electronic structures and unusually robust bandgap in an ultrahigh-mobility layered oxide semiconductor, $\text{Bi}_2\text{O}_2\text{Se}$. *Sci. Adv.* **4**, eaat8355 (2018).
- Wang, C., Ding, G. Q., Wu, X. M., Wei, S. S. & Gao, G. Y. Electron and phonon transport properties of layered $\text{Bi}_2\text{O}_2\text{Se}$ and $\text{Bi}_2\text{O}_2\text{Te}$ from first-principles calculations. *N. J. Phys.* **20**, 123014 (2018).
- Pereira, A. L. J. et al. Experimental and theoretical study of $\text{Bi}_2\text{O}_2\text{Se}$ under compression. *J. Phys. Chem. C* **122**, 8853–8867 (2018).
- An, J., Subedi, A. & Singh, D. J. Ab initio phonon dispersions for PbTe . *Sol. Stat. Comm.* **148**, 417–419 (2008).
- Kurita, K., Sakabayashi, H. & Okazaki, R. Correlation in transport coefficients of hole-doped CuRhO_2 single crystals. *Phys. Rev. B* **99**, 115103 (2019).
- Tsujii, N., Yoshimura, K. & Kosuge, K. Deviation from the Kadowaki–Woods relation in Yb-based intermediate-valence systems. *Matter* **15**, 1993–2003 (2003).
- Jaoui, A. et al. Departure from the Wiedemann–Franz law in WP_2 driven by mismatch in T -square resistivity prefactors. *npj Quant. Mat.* **3**, 64 (2018).
- Behni, K., Jaccard, D. & Flouquet, J. On the thermoelectricity of correlated electrons in the zero-temperature limit. *J. Phys. Cond. Mat.* **16**, 5187–5198 (2004).
- Mott, N.F. *Metal-Insulator Transitions* 2nd edn. (Taylor and Francis, London, 1990) pp. 72–73.
- Koshino, S. Scattering of electrons by the thermal motion of impurity ions. II. *Prog. Theor. Phys.* **24**, 1049–1054 (1960).
- Taylor, P. L. Changes in electrical resistance caused by incoherent electron-phonon scattering. *Phys. Rev.* **135**, A1333–A1335 (1964).
- Reizer, M. Y. & Sergeev, A. V. The effect of the electron-phonon interaction of the conductivity of impure metals. *Sov. Phys. JETP* **65**, 1291–1298 (1987).
- Pal, H. K., Yudson, V. I. & Maslov, D. L. Resistivity of non-Galilean-invariant Fermi- and non-Fermi liquids. *Lith. J. Phys.* **52**, 142–164 (2012).
- Paul, I. Interaction correction of conductivity near a ferromagnetic quantum critical point. *Phys. Rev. B* **77**, 224418 (2008).
- Giannozzi, P. et al. QUANTUM ESPRESSO: a modular and open-source software project for quantum simulations of materials. *J. Phys. Condens. Matter* **21**, 395502 (2009).
- Csonka, G. I. et al. Assessing the performance of recent density functionals for bulk solids. *Phys. Rev. B* **79**, 155107 (2009).
- Garrity, K. F., Bennett, J. W., Rabe, K. M. & Vanderbilt, D. Pseudopotentials for high-throughput DFT calculations. *Comput. Mater. Sci.* **81**, 446–452 (2014).
- Togo, A. & Tanaka, I. First principles phonon calculations in materials science. *Scr. Materialia* **108**, 1–5 (2015).
- Corso, A. D. Pseudopotentials periodic table: from H to Pu. *Comput. Mater. Sci.* **95**, 337–350 (2014).
- Sakai, A., Kanno, T., Yotsuhashi, S., Adachi, H. & Tokura, Y. Thermoelectric properties of electron-doped KTAO_3 . *Jpn. J. Appl. Phys.* **48**, 097002 (2009).
- Martino, E. et al. Two-dimensional conical dispersion in ZrTe_5 evidenced by optical spectroscopy. *Phys. Rev. Lett.* **122**, 217402 (2019).
- Maruhashi, K. et al. Anisotropic quantum transport through a single spin channel in the magnetic semiconductor EuTiO_3 . *Adv. Mater.* **32**, 1908315 (2020).

Acknowledgements

This research was supported by National Natural Science Foundation of China via Project 11904294, Zhejiang Provincial Natural Science Foundation of China under Grant No. LQ19A040005 and the foundation of Westlake University. We thank the support provided by Dr. Chao Zhang from Instrumentation and Service Center for Physical Sciences (ISCPS) and computational resource provided by Supercomputer Center in Westlake University. This work is part of a DFG-ANR project funded by Agence Nationale de la Recherche (ANR-18-CE92-0020-01) and by the DFG through projects LO 818/6-1 and HE 3219/6-1.

Author contributions

J.L.W. prepared the samples and did the experiments. He was assisted in the measurements by Z.K.X., J.F.W., W.H.H., and Z.R. J.W. and S.L. did DFT calculations. J.L.W., T.W., and X.L. prepared the figures. K.B. and X.L. wrote the manuscript. X.L. led the project. All authors contributed to the discussion.

Competing interests

The authors declare no competing interests.

Additional information

Supplementary information is available for this paper at <https://doi.org/10.1038/s41467-020-17692-6>.

Correspondence and requests for materials should be addressed to X.L.

Peer review information *Nature Communications* thanks Filip Ronning and the other, anonymous, reviewer(s) for their contribution to the peer review of this work. Peer reviewer reports are available.

Reprints and permission information is available at <http://www.nature.com/reprints>

Publisher's note Springer Nature remains neutral with regard to jurisdictional claims in published maps and institutional affiliations.



Open Access This article is licensed under a Creative Commons Attribution 4.0 International License, which permits use, sharing, adaptation, distribution and reproduction in any medium or format, as long as you give appropriate credit to the original author(s) and the source, provide a link to the Creative Commons license, and indicate if changes were made. The images or other third party material in this article are included in the article's Creative Commons license, unless indicated otherwise in a credit line to the material. If material is not included in the article's Creative Commons license and your intended use is not permitted by statutory regulation or exceeds the permitted use, you will need to obtain permission directly from the copyright holder. To view a copy of this license, visit <http://creativecommons.org/licenses/by/4.0/>.

© The Author(s) 2020